Article

Attosecond clocking of correlations between Bloch electrons

https://doi.org/10.1038/s41586-022-05190-2

Received: 23 February 2022

Accepted: 3 August 2022

Published online: 12 October 2022

Check for updates

J. Freudenstein[1,3], M. Borsch[2,3], M. Meierhofer[1], D. Afanasiev[1]✉, C. P. Schmid[1], F. Sandner[1], M. Liebich[1], A. Girnghuber[1], M. Knorr[1], M. Kira[2]✉ & R. Huber[1]✉

Delocalized Bloch electrons and the low-energy correlations between them determine key optical[1], electronic[2] and entanglement[3] functionalities of solids, all the way through to phase transitions[4,5]. To directly capture how many-body correlations affect the actual motion of Bloch electrons, subfemtosecond (1 fs = 10^{-15} s) temporal precision[6–15] is desirable. Yet, probing with attosecond (1 as = 10^{-18} s) high-energy photons has not been energy-selective enough to resolve the relevant millielectronvolt-scale interactions of electrons[1–5,16,17] near the Fermi energy. Here, we use multi-terahertz light fields to force electron–hole pairs in crystalline semiconductors onto closed trajectories, and clock the delay between separation and recollision with 300 as precision, corresponding to 0.7% of the driving field's oscillation period. We detect that strong Coulomb correlations emergent in atomically thin WSe_2 shift the optimal timing of recollisions by up to 1.2 ± 0.3 fs compared to the bulk material. A quantitative analysis with quantum-dynamic many-body computations in a Wigner-function representation yields a direct and intuitive view on how the Coulomb interaction, non-classical aspects, the strength of the driving field and the valley polarization influence the dynamics. The resulting attosecond chronoscopy of delocalized electrons could revolutionize the understanding of unexpected phase transitions and emergent quantum-dynamic phenomena for future electronic, optoelectronic and quantum-information technologies.

Attosecond science has created completely new possibilities for condensed-matter physics to directly follow electron motion on the shortest relevant time scales[6–15,18–23]. Precise timing of the photoelectric effect has been exploited to track electronic wave-packet motion[9,11,14,15], whereas transient absorption has revealed sub-fs bandgap dynamics[8,12], intraband currents[20] and screening[21]. Also, subcycle coherent energy transfer by strong optical fields in dielectrics has been investigated[7,10]. Going beyond single-particle dynamics, correlations within the same atom[14] and core excitons[13] have become accessible. Yet, the time–energy uncertainty of attosecond probes implies large bandwidths, from multiple to tens of electronvolts, which has limited the accessible energy resolution much above the millielectronvolt (meV) scale that governs key electronic correlation dynamics in solids.

Conversely, the meV photon energies of multi-terahertz (THz) pulses are perfectly matched to probe correlation-induced excitations[16,17]. Owing to the slow carrier field, ultrafast experiments need to be performed faster than a single oscillation period of the electromagnetic radiation. In fact, subcycle high-harmonic[24] and high-order sideband generation[25,26], transient absorption spectroscopy[27] and complete band structure movies[28] have unveiled lightwave-driven electron currents[25,26,28], dynamical Bloch oscillations[24] and localization[27] with sub-10 fs resolution. Light-field-accelerated electrons have also enabled all-optical reconstruction of band structures[29,30] and Bloch waves[31]. Yet, resolving the influence of correlation effects on the trajectories of delocalized Bloch electrons has remained an open challenge.

Van der Waals layered materials form an ideal test bed to explore electronic correlations[5,32–35]. In atomically thin monolayers of transition metal dichalcogenides (TMDCs), the extreme in-plane quantum confinement and suppressed screening in the third dimension give rise to large Coulomb correlations, binding photogenerated electron–hole (e–h) pairs into atom-like quasiparticles called excitons[32,36]. Being stable even above room temperature, these excitons determine key optoelectronic properties and form the basis for yet more complex many-body quasiparticles, such as trions, biexcitons[32] or dropletons[37]. Importantly, Coulomb correlations can be sensitively tuned by stacking monolayers; the exciton binding energy is strongly reduced in multilayer TMDC crystals[32,38], and twisted stacking has enabled tailoring of Mott insulators[33,34], Wigner crystal states[35] and superconductivity[5], among others.

Here, we reveal the effect of many-body interactions on the motion of delocalized electrons, directly in the time domain, by merging sub-fs resolution with meV energy selectivity. To this end, we direct e–h pairs in TMDC crystals onto closed recollision paths by intense THz carrier fields, and clock the precise timing by analysing the resulting high-order sideband (HSB) radiation. We push the experimental sensitivity to probe these dynamics, even in ultimately thin solids with a time resolution of 300 as, and connect the measured delays uniquely to Coulomb correlations via quantum theory.

[1]Department of Physics, University of Regensburg, Regensburg, Germany. [2]Department of Electrical Engineering and Computer Science, University of Michigan, Ann Arbor, MI, USA. [3]These authors contributed equally: J. Freudenstein, M. Borsch. ✉e-mail: dmytro.afanasiev@ur.de; mackkira@umich.edu; rupert.huber@ur.de

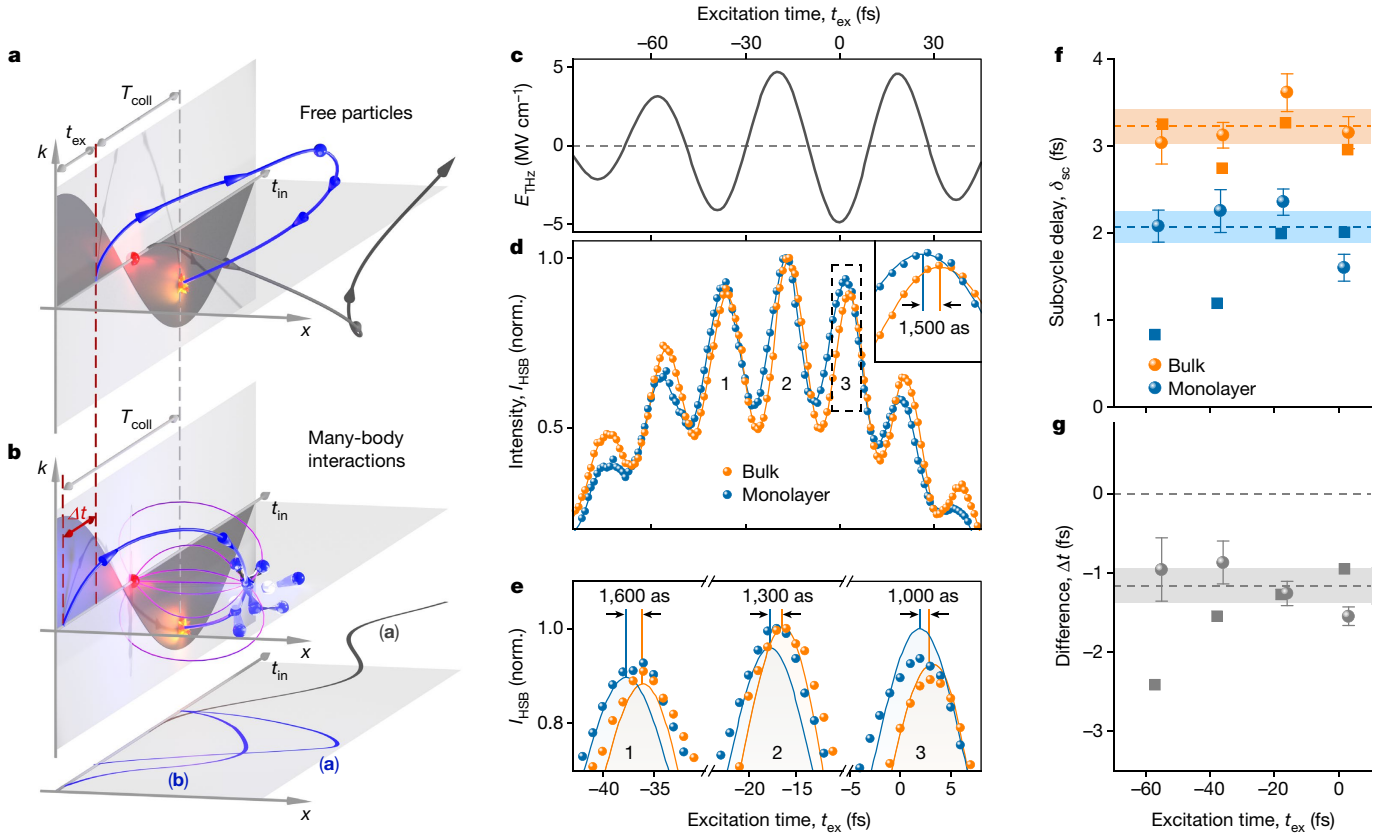

Fig. 1 | Clocking quasiparticle collisions in bulk and monolayer WSe_2. **a**,**b**, Schematic phase-space trajectories. An e–h pair created at excitation time t_{ex} is accelerated by the force exerted by an intense THz waveform (grey shaded area), which changes the e–h distance x and the relative crystal momentum $\hbar k$. Uncorrelated e–h pairs (**a**) generated shortly after a THz field crest recollide ballistically ($x = 0$) at a delay time T_{coll} (blue trajectory), emitting HSB radiation. Pairs created shortly after a zero-crossing of the THz field cannot recollide (grey trajectory) within their lifetime. Many-body interactions (**b**), such as excitonic e–h pair correlations (purple field lines) and scattering with other carriers (blue spheres), modify trajectories and reduce T_{coll}. Δt indicates the difference between optimum t_{ex} with and without many-body interactions. Bottom panel, projection of the trajectories in **a** and **b** onto the t_{in}–x plane. **c**, Experimental THz driving field (peak amplitude, 4.9 MV cm^{-1}) centred at 25 THz. **d**, Experimentally recorded spectrally integrated (energy window, 2.0 to 2.64 eV) HSB intensity, I_{HSB}, from bulk (thickness, 60 nm, orange) and monolayer WSe_2 (blue) as a function of t_{ex} defined by the delay between the NIR excitation pulse (fluence $\Phi_{NIR} = 14$ μJ cm^{-2}, linear polarization) and the THz driving field pointing along the K–$\bar{K}$ direction; solid lines are quadratic regressions; norm., normalized. Inset: zoomed-in view of dashed box in main panel with Gaussian fits (solid lines). **e**, Close-up of I_{HSB} maxima around $t_{ex} = -37$ fs (left, 1), $t_{ex} = -17$ fs (middle, 2) and $t_{ex} = 2$ fs (right, 3) compares experiment (spheres) with QDCE computations (shaded areas; relative heights as predicted/measured). The timing differences between bulk and monolayer as extracted from QDCE calculations are labelled. Bulk peaks are shifted towards positive delay times. **f**, Measured (spheres) and QDCE-computed (squares) subcycle delay δ_{sc} between optimal t_{ex} and nearest THz field crest in bulk (orange) and monolayer (blue) WSe_2. Dashed lines and shaded areas indicate peak-averaged values $\langle\delta_{sc}^{bulk}\rangle = 3.2 \pm 0.2$ fs and $\langle\delta_{sc}^{ML}\rangle = 2.1 \pm 0.2$ fs and the respective standard error. **g**, Measured (spheres) and QDCE-computed (squares) difference between optimal excitation times in bulk and monolayer WSe_2, Δt, for the data shown in **f** with a peak-averaged value $\Delta t = -1.2 \pm 0.3$ fs.

Attosecond Bloch-electron chronoscopy

Our clocking concept (Fig. 1a) uses the time grid formed by the oscillating carrier field of an intense, few-cycle THz pulse that transiently biases the crystal. At a tunable excitation time, t_{ex}, resonant interband transitions create coherent e–h pairs. When the generated pairs are separated by the THz-field induced force (grey shaded area), their distance x and relative momentum $\hbar k$ increase; when the THz field polarity subsequently flips during the lifetime τ of the e–h coherence, x and $\hbar k$ may decrease again. For favourable t_{ex}, the coherent e–h pairs recollide ($x = 0$) at a delay time T_{coll} after photogeneration (Fig. 1a, blue trajectory). The pairs can then annihilate, emitting their excess energy, set by $\hbar k$ at impact (Methods), as broadband HSB radiation. For less optimal t_{ex}, there will be no recollision (Fig. 1a, grey trajectory) within τ. By analysing the HSB radiation as a function of t_{ex}, one can identify the best timing for efficient recollisions.

Whereas quasi-free e–h pairs follow ballistic motion governed by the single-particle band structure (Fig. 1a), many-body correlations (Fig. 1b) such as excitonic binding (purple field lines) and interactions with other carriers (blue spheres) modify the trajectories and recollision times T_{coll}. Coulomb attraction, for instance, acts as a restoring force. To reach large relative momenta for high-energy recollisions, interacting e–h pairs must undergo an enhanced action of the THz field during the separation phase compared to free pairs (Methods). This can be achieved by optical excitation at earlier t_{ex} (Fig. 1b, blue trajectory). Overall, the distinct dynamics of free and correlated electrons should manifest in a shift Δt of the optimum t_{ex}, which can be probed experimentally. Because measuring delays between two field maxima is not restricted by the uncertainty principle, t_{ex} can be clocked to massively subcycle precision, limited only by the signal-to-noise ratio and the stability of the setup.

Clocking Coulomb correlations in TMDCs

The vastly different Coulomb interactions in bulk and monolayer TMDCs[32,38] offer the perfect benchmark for this concept. We

mechanically stamped a large-area WSe_2 monolayer next to bulk 2H-WSe_2 (thickness, 60 nm) on the same diamond substrate (Methods). The exciton binding energies (bulk, 60 meV; monolayer, approximately 0.3 eV) differ by up to a factor of five[32,38]. We first use linearly polarized near-infrared (NIR) pulses with a duration of 9 fs (fluence, $\Phi_{NIR} = 14\ \mu J\ cm^{-2}$) to create excitons. The high-energy edge of the NIR spectrum is resonant with the monolayer 1*s* A exciton (photon energy, 1.665 eV). The photogenerated *e*–*h* pairs are accelerated by a linearly polarized THz pulse (centre frequency, $\nu_{THz} = 25$ THz; peak field, $E_{peak} = 4.9\ MV\ cm^{-1}$; Fig. 1c); emerging HSB spectra are recorded as a function of t_{ex}. An active carrier-envelope-phase stabilization scheme and simultaneous electro-optic monitoring of the THz driving field (Methods) suppress temporal drift artefacts and enable resolution of attosecond shifts in t_{ex}, even in atomically thin crystals.

The measured spectrally integrated HSB intensity, I_{HSB} (Fig. 1d), of bulk (orange spheres) and monolayer (blue spheres) WSe_2 is strongly modulated as a function of t_{ex}. This corroborates the existence of good and bad excitation times for efficient recollisions; the former occur shortly after THz field crests (Fig. 1a,b). Most remarkably, all I_{HSB} maxima from the monolayer exhibit a systematic shift to earlier delays than for the bulk data (Fig. 1e). We accurately resolve the temporal position of the local maxima with Gaussian (Fig. 1d, inset) and quadratic regressions (Fig. 1d, main panel), with both yielding the same timing (Methods). For each THz half-cycle, we then extract the subcycle delay δ_{sc} between the field crest and the nearest maximum of I_{HSB} (Fig. 1f), as well as the shift $\Delta t = \delta_{sc}^{ML} - \delta_{sc}^{bulk}$ between the peaks of I_{HSB} from the monolayer (ML) and the bulk (Fig. 1g). A thorough analysis of the statistical and systematic measurement errors (Methods) yields a timing resolution of around 300 as (Fig. 1f,g, error bars). Thus, our experiment clocks good recollision events 130 times more accurately than the duration of a single THz period, that is, much better than the typical time-bandwidth limit. For all THz half-cycles, δ_{sc}^{ML} is significantly smaller than δ_{sc}^{bulk} (Fig. 1f), with a mean timing of the four largest I_{HSB} peaks of $\langle\delta_{sc}^{ML}\rangle = 2.1 \pm 0.2$ fs (Fig. 1f, blue dashed line) and $\langle\delta_{sc}^{bulk}\rangle = 3.2 \pm 0.2$ fs (orange dashed line). Consequently, the difference Δt is consistently negative (Fig. 1g, spheres) with a cycle-averaged value of -1.2 ± 0.3 fs.

Quantum predictions of subcycle dynamics

We perform rigorous quantum-dynamic cluster-expansion (QDCE) computations[36] to precisely predict I_{HSB} and firmly connect the measured delays with many-body correlations. The monolayer and bulk band structure alongside geometric phases over the full Brillouin zone are accounted for to systematically solve the intertwined effects of extreme lightwave excitations and many-body Coulomb interactions on HSB emission (Methods). Our QDCE computations quantitatively explain the experimental subcycle timing (Fig. 1e,f) and the distinctly negative Δt between monolayer and bulk samples (Fig. 1g). We confirmed that the changes of δ_{sc} are indeed dominated by the very different Coulomb correlations in bulk versus monolayer WSe_2 (Methods). Yet, the agreement between theory and experiment goes much further. The computed full two-dimensional I_{HSB} spectrogram from a WSe_2 monolayer as a function of photon energy and delay time t_{ex} (Fig. 2a, top) explains its experimental counterpart (Fig. 2a, bottom) in astonishing detail. Cross-sections through the spectrogram along the energy axis at fixed $t_{ex} = -19$ fs (Fig. 2b) and along the time axis at $h\nu = 2.06$ eV (Fig. 2c) illustrate this excellent congruence and provide us with important insights into the microscopic dynamics.

Notably, the computed I_{HSB} spectrum (Fig. 2b, orange line) predicts both the relative intensity of the HSB emission with respect to the incident excitation intensity I_{NIR} and the spectral shapes observed experimentally (grey area). In the full QDCE computations (orange line), state-dependent scattering[36] dephases the 1*s* A excitons with a decay time of $\tau = 21.9$ fs, which decreases to $\tau = 8.2$ fs once THz acceleration ionizes the excitons. By contrast, a simplified constant-dephasing

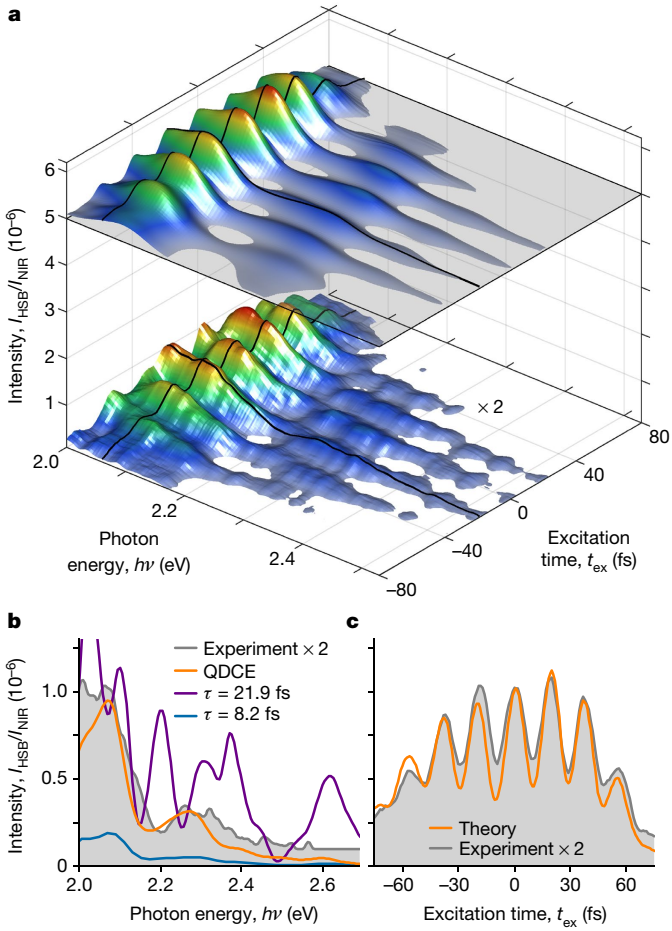

Fig. 2 | Quantitative many-body aspects in HSB spectra of monolayer WSe_2. **a**, Full HSB spectrogram from monolayer WSe_2 as a function of the delay time t_{ex}, for $E_{peak} = 6.2\ MV\ cm^{-1}$ and $\Phi_{NIR} = 9.5\ \mu J\ cm^{-2}$. The result of a QDCE computation (top) is compared with a corresponding measurement (bottom, scaled by a factor of 2). Both spectrograms are given in units of the incident NIR excitation pulse, I_{NIR}, and are vertically offset for clarity. Black curves illustrate cuts through the spectrogram shown in **b** and **c**. **b**, The measured HSB spectrum (grey) recorded at delay time $t_{ex} = -19$ fs is compared with the full QDCE computation (orange line) and phenomenological analyses with dephasing times $\tau = 21.9$ fs (purple) and $\tau = 8.2$ fs (blue). Only the full QDCE computation explains the experiments quantitatively. **c**, I_{HSB} as a function of the delay time t_{ex} at a fixed photon energy of 2.06 eV from full QDCE computations (orange) and experiment (grey).

model with $\tau = 21.9$ fs (purple line) fails to explain the measured spectral shapes (Methods); using $\tau = 8.2$ fs (blue line) quenches I_{HSB} by an order of magnitude compared to the experiment. Hence, strongly and dynamically changing Coulomb scattering during *e*–*h* acceleration critically influences I_{HSB} from the monolayer. The full QDCE computations also reproduce the experimental t_{ex} dependence remarkably well (Fig. 2c).

Because excitonic attraction competes with lightwave-driven charge separation, the relative strength of both forces should influence the recollision dynamics. To explore this scenario, we measure the average subcycle delay in bulk (Fig. 3a, orange spheres) and monolayer (blue spheres) WSe_2 for various peak fields, kept safely below the onset of high-harmonic generation[26] (Methods). The monotonic increase of $\langle\delta_{sc}\rangle$ with E_{peak} is well reproduced by our QDCE computations (solid lines). Increasing E_{peak} ionizes the excitonic coherence faster, which reduces the probability of recollision during the subsequent THz half-cycle. Thus, maximum I_{HSB} is reached if the excitons are excited closer to a field zero-crossing, that is at larger t_{ex}, explaining the observed $\langle\delta_{sc}\rangle$

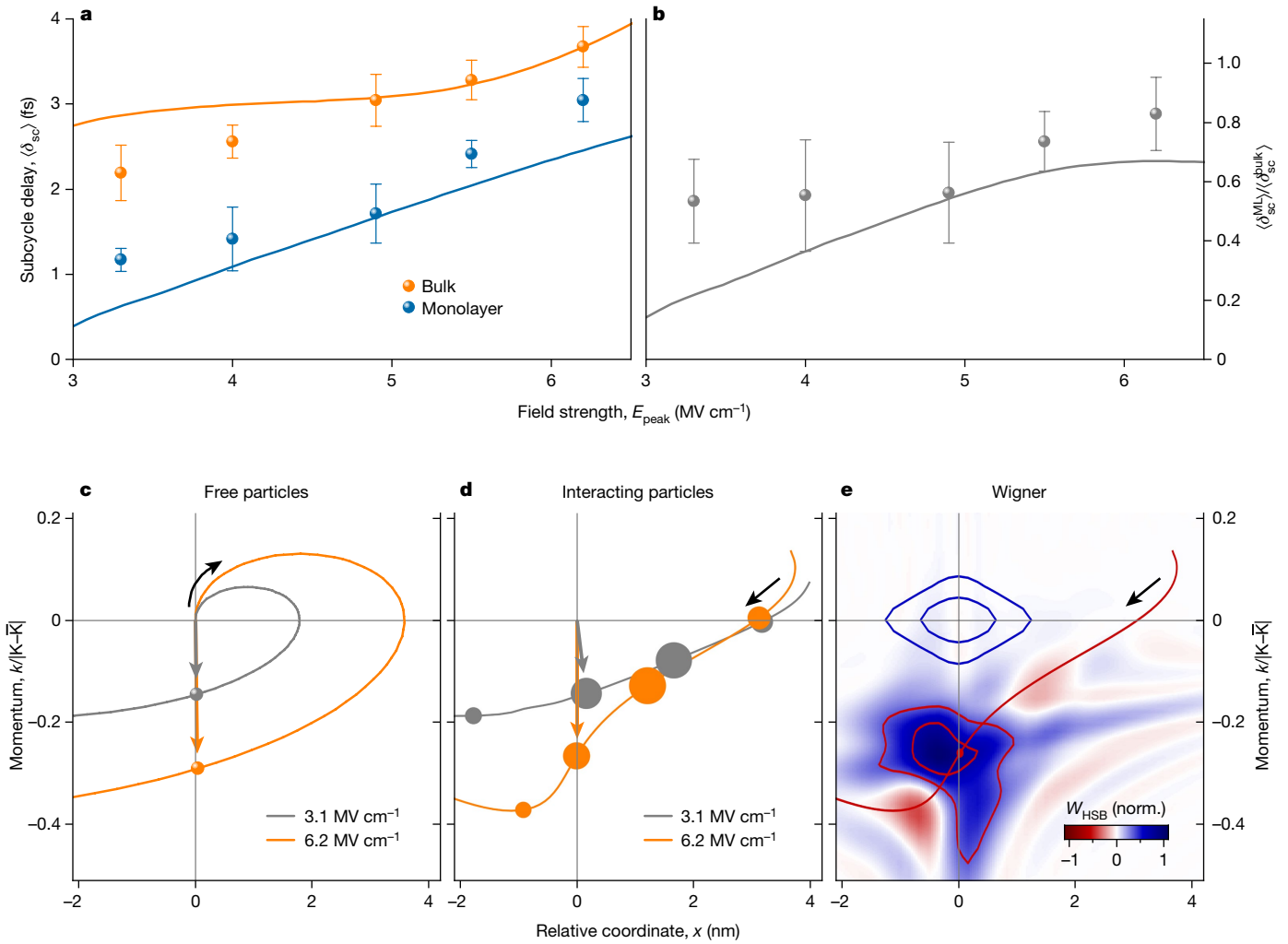

Fig. 3 | Exciton dynamics at different driving field strengths. a, Measured (spheres) and QDCE-computed (solid lines) subcycle delay $\langle\delta_{sc}\rangle$ (averaged over three peaks between $t_{ex} \approx -40$ fs and $t_{ex} \approx 0$ fs) and their respective standard error for bulk (orange) and monolayer WSe_2 (blue) as a function of the peak THz field strength E_{peak} of linearly polarized excitation ($\Phi_{NIR} = 9.5$ μJ cm^{-2}), corresponding to 10^{12} cm^{-2} injected carriers. **b**, Measured (spheres) and QDCE-computed (solid line) ratio of bulk and monolayer subcycle delay for the data shown in **a**. **c**,**d**, Computed trajectories of non-interacting e–h pairs in a parabolic band (**c**) and correlated excitons in monolayer WSe_2 (**d**) excited at $t_{ex} = -16.5$ fs and accelerated by lightwaves with peak fields of $E_{peak} = 3.1$ MV cm^{-1} (grey) and $E_{peak} = 6.2$ MV cm^{-1} (orange). Grey and orange arrows mark the (x, k) coordinates at elapsed times of 20.9 fs (**c**) and 15.9 fs (**d**), which correspond to the respective recollision times for $E_{peak} = 6.2$ MV cm^{-1}. Free particles in a parabolic band (**c**) feature $\delta_{sc} = 2.0$ fs for $\nu_{THz} = 25$ THz. The diameters of the circles in **d** correspond to the excitonic polarization contributing to I_{HSB}. Black arrows in **c** and **d** indicate the temporal direction of the trajectories. **e**, Spectrally filtered Wigner function $W_{HSB}(x,k)$ for $E_{peak} = 6.2$ MV cm^{-1} during the recollision. Blue contours denote the Wigner function of the 1*s* exciton state, red the equivalent contours for the recolliding state.

trend. A transient version of this effect is also detected in Fig. 1c–f, in which δ_{sc} tends to increase towards the central half-cycles. The strongest fields ultimately render the different Coulomb correlations in bulk and monolayer crystals irrelevant and level the corresponding dynamics. In fact, the ratio of bulk and monolayer delays $\langle\delta_{sc}^{ML}\rangle/\langle\delta_{sc}^{bulk}\rangle$ approaches unity as E_{peak} increases to dominate the Coulomb forces (Fig. 3b).

To intuitively visualize how microscopic dynamics affect the HSBs, we represent the e–h coherences via a phase-space distribution whose centre of gravity determines an (x, k) trajectory. Its filtered version, $W_{HSB}(x, k)$, includes only energies above the fourth HSB (Methods) to determine the effect of correlations on (x, k) and to track the distribution details of the HSB-relevant processes. For free e–h pairs in a parabolic band, Fig. 3c shows two exemplary centre-of-gravity trajectories for field strengths of 3.1 MV cm^{-1} and 6.2 MV cm^{-1} and $t_{ex} = -16.5$ fs. Arrows indicating the phasors at the e–h recollision time $T_{coll} = 20.9$ fs after excitation are synchronized for the two cases, such that no field dependence of the subcycle delay is expected. According to Fig. 1b, many-body correlations should modify the trajectories and T_{coll}; we extract them from QDCE computations of $W_{HSB}(x, k)$ (Fig. 3d) with the same t_{ex} as for the free e–h pairs. The excitonic polarization contributing to I_{HSB} (diameter of the circles) initially increases as the e–h pairs gain kinetic energy, followed by a fast decay due to scattering and recollisions. Coulomb attraction and scattering not only reduce T_{coll}, but also introduce a field dependence. Doubling E_{peak} from 3.1 MV cm^{-1} (grey) to 6.2 MV cm^{-1} (orange) alters the trajectories and reduces T_{coll} from 16.2 fs to 15.9 fs (see misaligned arrows at the elapsed time of 15.9 fs). Unlike in the non-interacting case (Fig. 3c), δ_{sc} thus varies with the field strength, as observed in Fig. 3a.

Despite the intuitive picture obtained from the centre-of-gravity (x, k) trajectory, our theory carries much more depth in the full Wigner function $W_{HSB}(x, k)$. Starting from a symmetric distribution of coherent 1*s* excitons (Fig. 3e, blue contours) at t_{ex}, the Wigner function becomes strongly structured. Figure 3e displays $W_{HSB}(x, k)$ when

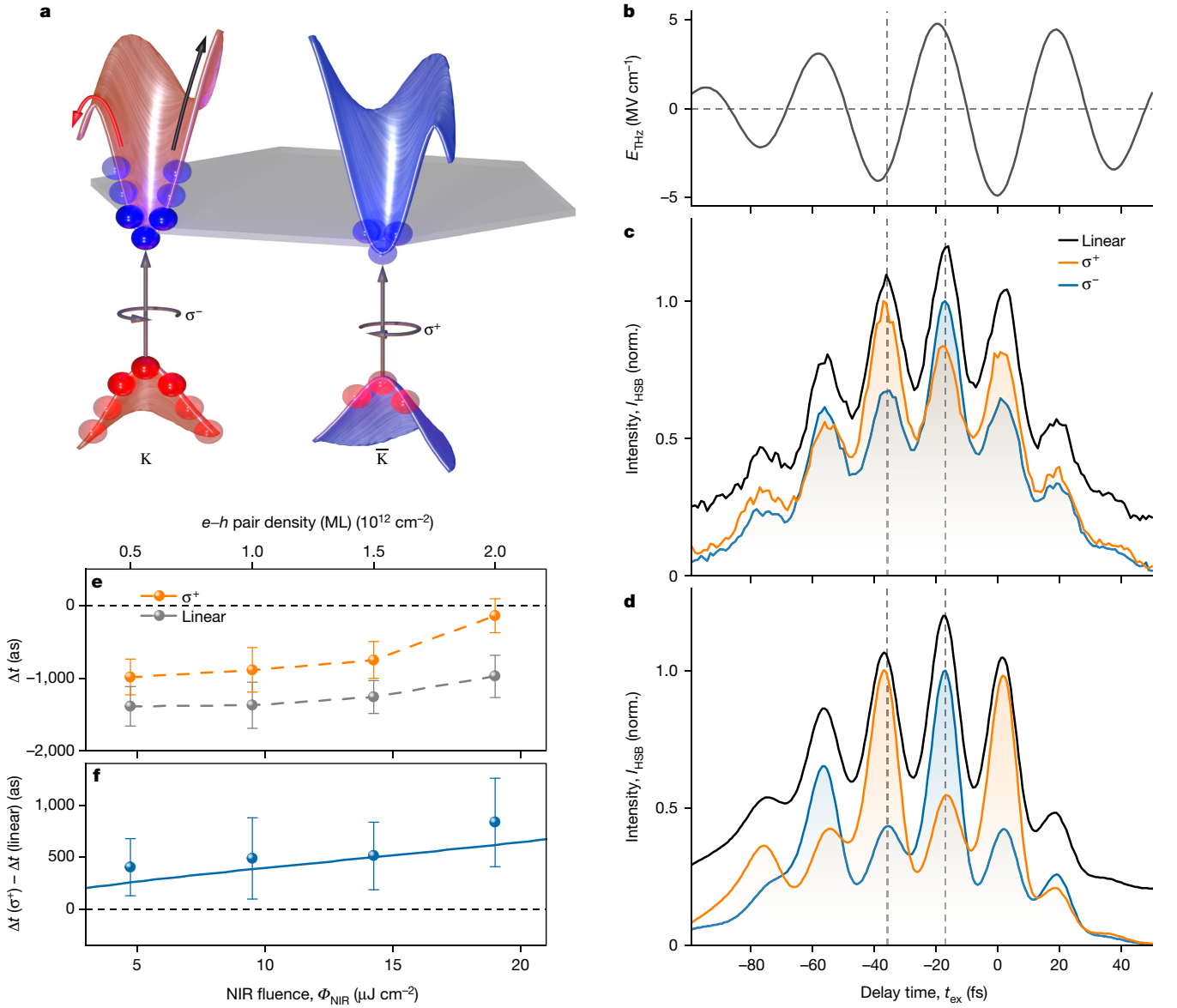

Fig. 4 | Attosecond timing of correlations in valley-polarized *e*–*h* pairs. **a**, Schematic of the conduction- and valence-band structure (red and blue surface) of monolayer WSe_2, in which a left (σ^-) or right (σ^+) circularly polarized NIR pulse selectively excites coherent excitons in the K or $\overline{K}$ valley, respectively. The band structure of one specific valley along the K–$\overline{K}$ direction is asymmetric, leading to different dynamics for *e*–*h* pairs (blue and red spheres) when accelerated in opposite directions (red and black arrows). Applying a linearly polarized NIR pulse excites equal K and $\overline{K}$ populations (transparent spheres in the $\overline{K}$ valley). Exciting *e*–*h* pairs (spheres) into only one specific valley enhances Pauli blocking. **b**, Terahertz driving field centred at 25 THz. **c**,**d**, Measured (**c**) versus computed (**d**), spectrally integrated I_{HSB} (between 2.18 and 2.64 eV) from monolayer WSe_2 using right circularly (orange), left circularly (blue) and linearly (black, vertically displaced for clarity) polarized excitation (Φ_{NIR} = 14 μJ cm^{-2}) as a function of t_{ex}. **e**, Averaged subcycle delay difference, $\Delta t = \langle \delta_{sc}^{ML} \rangle - \langle \delta_{sc}^{bulk} \rangle$ (averaged over five peaks between $t_{ex} \approx -60$ fs and $t_{ex} \approx 20$ fs) and their respective standard error, measured between bulk and ML for linear (grey spheres) and right circularly polarized excitation (orange spheres) as a function of Φ_{NIR}; the corresponding *e*–*h* densities are presented in the upper axis. **f**, The averaged measured (spheres) and QDCE-computed (solid line) subcycle delay difference, $\Delta t(\sigma^+) - \Delta t$(linear) determined from the right circularly and linearly polarized excitation presented in **e**, becomes $\langle \delta_{sc}^{ML} \rangle (\sigma^+) - \langle \delta_{sc}^{ML} \rangle$ (linear) because the bulk dynamics exhibit only a weak Φ_{NIR} dependence.

its centre (Fig. 3e, red circle) matches the recollision point (0, *k*) for E_{peak} = 6.2 MV cm^{-1}. The combination of lightwave acceleration and many-body effects not only changes the overall phasor shape, but also creates significant negative parts as a definite signature of quantum features beyond semiclassical descriptions.

Many-body excitation effects

Attosecond chronoscopy can even sense intricate quantum details of electrons, such as the valley pseudospin[39,40]. In monolayer TMDCs, strong spin–orbit interaction and broken inversion symmetry allow left (σ^-) and right (σ^+) circularly polarized NIR pulses to selectively populate the opposite K and $\overline{K}$ valleys in momentum space, respectively (Fig. 4a). As the band structure along the K – $\overline{K}$ direction is asymmetric (Fig. 4a, red and black arrows), the *e*–*h* trajectory depends on the combination of the THz field polarity (Fig. 4b) and the starting point of the trajectory (Fig. 4c). Generating *e*–*h* pairs with σ^- (σ^+) excitation during positive (negative) half-cycles of the driving field yields stronger I_{HSB} than during half-cycles of opposite polarity. Our QDCE computations confirm this alternating structure (Fig. 4d) because *e*–*h* acceleration towards the steeper increase of the band energy causes higher energy recollisions. For linearly polarized excitation, equal population of the

mirror-symmetric K and $\overline{K}$ points adds up to a symmetric response for positive and negative THz fields (Fig. 4c,d).

Additionally, many-body correlations should leave characteristic timing imprints because the valley polarization can be exploited to switch the strength of the Coulomb interaction $V_{\mathbf{k},\mathbf{k}'}$ between electrons at wave vectors $\mathbf{k}$ and $\mathbf{k}'$. Specifically, the presence of electrons at $\mathbf{k}$ effectively reduces $V_{\mathbf{k},\mathbf{k}'}$ via Pauli blocking[36], which prohibits fermions from occupying the same $\mathbf{k}$ state (Methods). Such a reduction is expected to be particularly strong in monolayer samples when circularly polarized light excites e–h pairs and blocks $\mathbf{k}$ states only in a single valley. Indeed, we find that Δt is significantly less negative (Fig. 4e), corresponding to a stronger reduction of $V_{\mathbf{k},\mathbf{k}'}$ for circular than for linear polarization. For large excitation fluences, Δt approaches zero—the quasi-free limit for the bulk. We verified that $\langle \delta_{sc}^{bulk} \rangle$ (linear) does not change for the excitation levels studied here. To quantify the contrast between strong and weak Pauli blocking induced by circularly versus linearly polarized excitation, we analyse the difference Δt (σ^+) − Δt (linear) (Fig. 4f). Both measurements (spheres) and full QDCE computations (solid line) produce a monotonic increase from 250 as to 750 as with increasing Φ_{NIR}, confirming that Pauli blocking switches the attosecond timing of recollisions. Our computations predict that δ_{sc} could even resolve correlation changes associated with the Mott transition from excitons to an electron–hole plasma.

Conclusion and outlook

Attosecond clocking of delocalized Bloch electrons reveals many-body correlations in a completely new way—directly in the time domain—as demonstrated by correlation tuning in TMDC monolayers and bulk crystals. Our concept is based on forcing e–h pairs onto THz-driven recollision paths and tracking the ideal excitation timing with centicycle precision with respect to the THz period. The presented, comprehensive theory–experiment comparisons identify distinct valley pseudospin and correlation signatures resulting directly from strong excitonic Coulomb attraction, excitation-induced dephasing and Pauli-blocking effects, all resolved down to the subfemtosecond scale. Yet, ultrafast chronoscopy of low-energy correlations opens a much broader perspective: deciphering tailored correlation dynamics in artificial van der Waals heterostructures or naturally occurring correlated states in quantum materials could revolutionize the access to emergent quantum dynamics, phases and topology. Exploring the intrinsic speed limits of electronic dynamics is also key to ultimately fast future lightwave electronics, optoelectronics and quantum-information processing.

Online content

Any methods, additional references, Nature Research reporting summaries, source data, extended data, supplementary information, acknowledgements, peer review information; details of author contributions and competing interests; and statements of data and code availability are available at https://doi.org/10.1038/s41586-022-05190-2.

1. Basov, D. N., Averitt, R. D., van der Marel, D., Dressel, M. & Haule, K. Electrodynamics of correlated electron materials. *Rev. Mod. Phys.* **83**, 471–541 (2011).
2. Spencer, J. Learning many-electron wavefunctions with deep neural networks. *Nat. Rev. Phys.* **3**, 458 (2021).
3. Scappucci, G. et al. The germanium quantum information route. *Nat. Rev. Mat.* **6**, 926–943 (2021).
4. Basov, D. N., Averitt, R. D. & Hsieh, D. Towards properties on demand in quantum materials. *Nat. Mater.* **16**, 1077–1088 (2017).
5. Cao, Y. et al. Unconventional superconductivity in magic-angle graphene superlattices. *Nature* **556**, 43–50 (2018).
6. Cavalieri, A. L. et al. Attosecond spectroscopy in condensed matter. *Nature* **449**, 1029–1032 (2007).
7. Schultze, M. et al. Controlling dielectrics with the electric field of light. *Nature* **493**, 75–78 (2013).
8. Schultze, M. et al. Attosecond band-gap dynamics in silicon. *Science* **346**, 1348–1352 (2014).
9. Neppl, S. et al. Direct observation of electron propagation and dielectric screening on the atomic length scale. *Nature* **517**, 342–346 (2015).
10. Sommer, A. et al. Attosecond nonlinear polarization and light–matter energy transfer in solids. *Nature* **534**, 86–90 (2016).
11. Tao, Z. et al. Direct time-domain observation of attosecond final-state lifetimes in photoemission from solids. *Science* **353**, 62–67 (2016).
12. Lucchini, M. et al. Attosecond dynamical Franz–Keldysh effect in polycrystalline diamond. *Science* **353**, 916–919 (2016).
13. Moulet, A. et al. Soft X-ray excitonics. *Science* **357**, 1134–1138 (2017).
14. Siek, F. et al. Angular momentum-induced delays in solid-state photoemission enhanced by intra-atomic interactions. *Science* **357**, 1274–1277 (2017).
15. Ossiander, M. et al. Absolute timing of the photoelectric effect. *Nature* **561**, 374–377 (2018).
16. Kampfrath, T., Tanaka, K. & Nelson, K. A. Resonant and nonresonant control over matter and light by intense terahertz transients. *Nat. Photon.* **7**, 680–690 (2013).
17. Dhillon, S. S. et al. The 2017 terahertz science and technology roadmap. *J. Phys. D.* **50**, 043001 (2017).
18. Ciappina, M. F. et al. Attosecond physics at the nanoscale. *Rep. Prog. Phys.* **80**, 054401 (2017).
19. Seiffert, L. et al. Attosecond chronoscopy of electron scattering in dielectric nanoparticles. *Nat. Phys.* **13**, 766–770 (2017).
20. Schlaepfer, F. et al. Attosecond optical-field-enhanced carrier injection into the GaAs conduction band. *Nat. Phys.* **14**, 560–564 (2018).
21. Volkov, M. et al. Attosecond screening dynamics mediated by electron localization in transition metals. *Nat. Phys.* **15**, 1145–1149 (2019).
22. Heide, C. et al. Attosecond-fast internal photoemission. *Nat. Photon.* **14**, 219–222 (2020).
23. Hui, D. et al. Attosecond electron motion control in dielectric. *Nat. Photon.* **16**, 33–37 (2022).
24. Hohenleutner, M. et al. Real-time observation of interfering crystal electrons in high-harmonic generation. *Nature* **523**, 572–575 (2015).
25. Zaks, B., Liu, R. B. & Sherwin, M. S. Experimental observation of electron–hole recollisions. *Nature* **483**, 580–583 (2012).
26. Langer, F. et al. Lightwave-driven quasiparticle collisions on a subcycle timescale. *Nature* **533**, 225–229 (2016).
27. Schmidt, C. et al. Signatures of transient Wannier–Stark localization in bulk gallium arsenide. *Nat. Commun.* **9**, 2890 (2018).
28. Reimann, J. et al. Subcycle observation of lightwave-driven Dirac currents in a topological surface band. *Nature* **562**, 396–400 (2018).
29. Vampa, G. et al. All-optical reconstruction of crystal band structure. *Phys. Rev. Lett.* **115**, 193603 (2015).
30. Borsch, M. et al. Super-resolution lightwave tomography of electronic bands in quantum materials. *Science* **370**, 1204–1207 (2020).
31. Costello, J. B. et al. Reconstruction of Bloch wavefunctions of holes in a semiconductor. *Nature* **599**, 57–61 (2021).
32. Wang, G. et al. Colloquium: excitons in atomically thin transition metal dichalcogenides. *Rev. Mod. Phys.* **90**, 021001 (2018).
33. Tang, Y. et al. Simulation of Hubbard model physics in WSe_2/WS_2 moiré superlattices. *Nature* **579**, 353–358 (2020).
34. Xu, Y. et al. Correlated insulating states at fractional fillings of moiré superlattices. *Nature* **587**, 214–218 (2020).
35. Zhou, Y. et al. Bilayer Wigner crystals in a transition metal dichalcogenide heterostructure. *Nature* **595**, 48–52 (2021).
36. Kira, M. & Koch, S. W. *Semiconductor Quantum Optics* (Cambridge Univ. Press, 2012).
37. Almand-Hunter, A. E. et al. Quantum droplets of electrons and holes. *Nature* **506**, 471–475 (2014).
38. Poellmann, C. et al. Resonant internal quantum transitions and femtosecond radiative decay of excitons in monolayer WSe_2. *Nat. Mater.* **14**, 889–893 (2015).
39. Xu, X., Yao, W., Xiao, D. & Heinz, T. F. Spin and pseudospins in layered transition metal dichalcogenides. *Nat. Phys.* **10**, 343–350 (2014).
40. Langer, F. et al. Lightwave valleytronics in a monolayer of tungsten diselenide. *Nature* **557**, 76–80 (2018).

Publisher's note Springer Nature remains neutral with regard to jurisdictional claims in published maps and institutional affiliations.

Springer Nature or its licensor holds exclusive rights to this article under a publishing agreement with the author(s) or other rightsholder(s); author self-archiving of the accepted manuscript version of this article is solely governed by the terms of such publishing agreement and applicable law.

© The Author(s), under exclusive licence to Springer Nature Limited 2022

Methods

Experimental setup

A femtosecond titanium-sapphire laser amplifier (repetition rate, 3 kHz) pumps a dual optical parametric amplifier (OPA), generating two individually tunable signal pulses with a centre wavelength of 1.2 μm and 1.33 μm, respectively. Being seeded by the same white-light continuum, the two pulses feature the same carrier-envelope phase (CEP) fluctuations. By difference frequency mixing between them in a GaSe crystal (thickness, 430 μm), we obtain a passively phase-stable THz pulse train (centre frequency, 25 THz; intensity full width at half maximum, 100 fs; pulse energy, 5 μJ). Thermal drifts of the exact optical path of the two signal branches could cause a slow modulation of the THz CEP. To stabilize the THz waveform against such long-term drifts, we implement a new active stabilization scheme. We split off a small fraction of the optical power of the two co-propagating cross-polarized signal pulses and select the spectral overlap between them with a 10 nm bandpass filter centred at 1,250 nm. A relative delay between the two pulses leads to a continuous shift of the polarization state of their superposition between linear and circular, which is evaluated by a quarter-wave plate, a Wollaston prism and two balanced photodiodes. In this way, relative drifts of the OPA arms are interferometrically detected and automatically corrected for by a delay stage, reducing the remaining CEP fluctuations of the THz waveforms to 28 mrad (ref. [41]).

Extended Data Fig. 1a shows a sketch of our experimental setup. The ultrashort excitation pulse, generated by compressing a white-light continuum from a YAG window, is characterized with second-harmonic frequency-resolved optical gating (SHG-FROG). Extended Data Fig. 1b shows the measured FROG trace from which we retrieve a pulse duration of 8.6 fs (Extended Data Fig. 1c). The excitation pulse is overlapped with the THz pulse using an indium tin oxide-coated window, and both are subsequently focused into the sample. The excitation and THz beams feature focal diameters of 22 μm and 60 μm (intensity full width at half maximum), respectively. For a sample, we can choose from either a WSe_2 (bulk or monolayer) crystal, for HSB generation, or a 500-nm-thick GaSe crystal, for electro-optic sampling (EOS) of the THz waveform. Both crystals are stamped on the same diamond substrate, which can be moved in the focal plane with micrometre precision using a motorized two-dimensional positioning stage. To selectively excite 1*s* excitons in the monolayer, the high-energy edge of the excitation spectrum (Extended Data Fig. 1d, orange curve) is chosen to coincide with this transition, which was verified by measuring the absorbance of the monolayer (Extended Data Fig. 1d, blue curve). Owing to the weaker excitonic binding energy in the bulk sample, our generation pulses can spectrally overlap with other exciton levels. Yet, the larger oscillator strength of the 1*s* state ensures that these coherences are generated more efficiently than the higher lying ones. Because the latter feature weaker correlations, they further contribute to the contrast in the strength of the interactions between bulk and monolayer. The sample is kept in ambient air and illuminated under normal incidence. Transmitted light and emerging HSB radiation are collimated with a parabolic mirror; the remaining THz radiation is separated from near-infrared to ultraviolet light with a germanium wafer. Using a dichroic mirror with a cut-off wavelength of 650 nm, the HSB radiation is coupled into a spectrometer, whereas the polarization state of low-energy light is analysed by an EOS detection unit. All spectra are corrected for the grating and CCD efficiency and all THz waveforms are corrected for the EOS detector response. With this scheme, we can conveniently switch between measuring HSB emission and detecting the THz waveform in the same sample focus by simply switching between the GaSe and the WSe_2 crystal with the motorized stage. By overlapping the THz pulse after the first focus with a copy of the ultrashort NIR pulse, we can simultaneously monitor the EOS signal of the driving field with a 5-μm-thick GaSe crystal, while measuring HSB generation in the sample focus. This enables us to monitor possible remaining instabilities of the experimental setup, which are typically as low as 84 as (Extended Data Fig. 1e).

Sample preparation

The WSe_2 sample, which consists of a monolayer and a bulk part, is exfoliated and transferred onto a diamond substrate using visco-elastic stamping (Extended Data Fig. 2a). Its crystalline orientation was determined by polarization-resolved second-harmonic generation. Placing the diamond substrate on an x–y translation stage enables mechanical positioning in the sample focus with micrometre precision. This way, the transmission of a 532 nm continuous-wave laser (Extended Data Fig. 2b, blue colour map) can be scanned over the sample and compared to the optical microscopy image to unambiguously identify different regions of interest. The thickness of the bulk part is determined using atomic force microscopy, revealing areas with 25 nm (Extended Data Fig. 2a, red part, right side of the sample) and 60 nm (blue part, bottom side of the sample) thickness. Next to the bulk area, the monolayer can be localized by measuring strong photoluminescence on illumination with the 532 nm continuous-wave laser (Extended Data Fig. 2b, red colour map), which additionally attests to the high sample quality. Extended Data Fig. 2c illustrates a schematic cross-section of our fabricated sample. The incident NIR and THz pulses first hit the WSe_2 sample and generate HSB radiation, which is then transmitted through the diamond substrate.

Propagation effects

For a quantitative comparison between bulk and monolayer subcycle delays, it is mandatory to place all relevant samples in the THz focus at the precisely same longitudinal position, to avoid apparent time shifts by a finite Gouy phase shift. Because bulk and monolayer sections of the sample are part of the same crystal, the lateral distance between them is less than 200 μm, and the diamond substrate is oriented exactly perpendicular to the laser beams, we estimate remaining variations of the Gouy phase to affect the extracted subcycle delay times by no more than 45 as. Additionally, we verified that linear and non-linear propagation effects inside bulk WSe_2 do not distort our findings. To this end, we performed HSB measurements on different spots of the bulk crystal with different thicknesses. Two typical sample areas with thicknesses of 60 nm and 25 nm (Extended Data Fig. 3) show peak-averaged subcycle delays of $\langle\delta_{sc}^{bulk}\rangle = 4.0 \pm 0.2$ fs and 4.1 ± 0.3 fs, respectively; the expected small difference in propagation times of 90 as between the 60-nm- and the 25-nm-thick bulk WSe_2 is well below the error margins. Thus, propagation effects can be ruled out as the source of our observed attosecond shift between bulk and monolayer samples.

Data analysis

To link the timing of the driving field with the most efficient injection time for HSB emission, we determine the temporal shape of the THz pulse by electro-optic sampling (Extended Data Fig. 4a) before (orange) and after (blue solid line) each scan of the HSB spectrogram. Drifts as small as 10 as can be detected by correlating the two THz waveforms and are subsequently corrected by shifting the time scales accordingly (see inset). Assuming a linear drift over a full measurement, these drifts can also be compensated in the HSB emission (Extended Data Fig. 4b, orange), to first order, by introducing a linear adjustment for the timescale (Extended Data Fig. 4b, blue). Depending on whether the waveform after the measurement has moved towards positive or negative delay times, the time axis for the HSB emission is stretched or squeezed, respectively.

We then determine the temporal position of the THz field crests and the local maxima of I_{HSB} (Extended Data Fig. 4c). For the latter, Gaussian fits (orange) over a range of 12 fs around each emission maximum (orange shaded areas) are used. Alternatively, we interpolate the measured I_{HSB} using a local quadratic regression (Extended Data Fig. 4e) and then fit its local maxima. By calculating the difference between the interpolated and measured I_{HSB} of Extended Data Fig. 4, we find a standard deviation of 1.1% corresponding to a noise-limited

time resolution of 100 as (see inset). The extracted timing (orange dashed line) is compared to the nearest driving field crest (grey dashed line), which yields the subcycle delay δ_{sc}. Each scan is typically repeated four times. Extended Data Fig. 4d,f shows the measured subcycle delay for four exemplary single scans (coloured spheres). By averaging, we end up with expectation values (blue spheres) for the subcycle delay of all four local I_{HSB} maxima considered here. Error bars correspond to the standard error of the mean value. When presenting peak-averaged values for the subcycle delay $\langle\delta_{sc}\rangle$, we average the individual error bars for the combined error margin. For constructing the error bars of the difference Δt, we first take the difference of the subcycle delays and subsequently retrieve their standard error accordingly.

QDCE theory

Extreme non-linear aspects of HSB generation stem from the interplay of strong Coulomb coupling among photo-excited electron–hole coherences and the simultaneous lightwave acceleration of e–h pairs that eventually recollide to emit HSBs. To predict HSB effects quantitatively, many-body effects, as well as the transport by the lightwave must be included at the same rigorous level, completely non-perturbatively. Our QDCE[36] approach is ideally suited for quantitatively predicting HSB effects because they result from a non-perturbative, strictly sequential build-up of many-body[42,43] and light–matter correlations[36,44], which the QDCE describes exactly.

In our experiments, the NIR pulse first generates single-particle quantities, so-called singlets such as the microscopic polarization $P_{\mathbf{k}}$ and the electron (hole) occupations $f_{\mathbf{k}}^{e(h)}$ at wave vector $\mathbf{k}$ before the onset of two-body correlations. Among the two bands with excitations, the exact singlet dynamics follows from the semiconductor Bloch equations (SBEs)[36]:

$$i\hbar\frac{\partial}{\partial t}P_{\mathbf{k}} = (\tilde{E}_{\mathbf{k}} + i\,|e|\mathbf{E}(t)\cdot\nabla_{\mathbf{k}} + \mathcal{A}_{\mathbf{k}}^{e,h}\cdot\mathbf{E}(t))P_{\mathbf{k}} + [1-f_{\mathbf{k}}^{e}-f_{\mathbf{k}}^{h}]\Omega_{\mathbf{k}} + \Gamma_{\mathbf{k}},$$

$$\hbar\frac{\partial}{\partial t}f_{\mathbf{k}}^{e(h)} = 2\mathrm{Im}[\Omega_{\mathbf{k}}^{*}P_{\mathbf{k}}] + |e|\mathbf{E}(t)\cdot\nabla_{\mathbf{k}}f_{\mathbf{k}}^{e(h)} + \Gamma_{\mathbf{k}}^{e(h)}, \quad (1)$$

which we couple to the wave equation of the electric field $\mathbf{E}$ to solve the self-consistent light absorption and emission, as discussed in ref. [42]. The total field $\mathbf{E}(t) = \mathbf{E}_{NIR}(t) + \mathbf{E}_{THz}(t)$ is a sum of the NIR pulse, $\mathbf{E}_{NIR}(t)$, exciting the singlets, and the THz field, $\mathbf{E}_{THz}(t)$, translating them within the bands. The band structure details of WSe_2 enter the renormalized e–h and Rabi energies

$$\tilde{E}_{\mathbf{k}} = E_{\mathbf{k}} - \sum_{\mathbf{k}'}(V_{\mathbf{k},\mathbf{k}}^{e,e}f_{\mathbf{k}'}^{e} + V_{\mathbf{k},\mathbf{k}}^{h,h}f_{\mathbf{k}'}^{h}),\ \Omega_{\mathbf{k}} = \mathbf{d}_{\mathbf{k}}^{e,h}\cdot\mathbf{E}(t) + \sum_{\mathbf{k}'}V_{\mathbf{k},\mathbf{k}'}^{e,h}P_{\mathbf{k}'}, \quad (2)$$

respectively, including the free e–h energy $E_{\mathbf{k}}$, the interband dipole matrix elements $\mathbf{d}_{\mathbf{k}}^{e,h}$, the gauge-dependent Berry connection $\mathcal{A}_{\mathbf{k}}^{e,h}$ and the Coulomb matrix elements $V_{\mathbf{k},\mathbf{k}}^{\lambda,\lambda'}$ for different combinations of the electron ($\lambda,\lambda' = e$) and hole ($\lambda,\lambda' = h$) bands. The singlet dynamics couple also to $\Gamma_{\mathbf{k}}$ and $\Gamma_{\mathbf{k}}^{e(h)}$, which contain microscopic two-particle correlations, so-called doublets, caused by interactions. The explicit doublet equations are given—for example in ref. [42]—and we find that systematic many-body scattering dynamics yields a lifetime of $\tau = 21.9$ fs for the 1s A exciton state in the monolayer, whereas higher exciton states dephase significantly faster, as discussed in the main text.

All matrix elements are computed ab initio using the relationships $\mathbf{d}_{\mathbf{k}}^{\lambda,\mu} = |e|\langle\phi_{\lambda,\mathbf{k}}|i\nabla_{\mathbf{k}}|\phi_{\mu,\mathbf{k}}\rangle$, $\mathcal{A}_{\mathbf{k}}^{e,h} = \mathbf{d}_{\mathbf{k}}^{e,e} - \mathbf{d}_{\mathbf{k}}^{h,h}$ and $V_{\mathbf{k},\mathbf{k}'}^{\lambda,\mu} = V_{\mathbf{k},\mathbf{k}'}\langle\phi_{\lambda,\mathbf{k}}|\phi_{\lambda,\mathbf{k}'}\rangle\langle\phi_{\mu,\mathbf{k}'}|\phi_{\mu,\mathbf{k}}\rangle$, where the single-particle wave functions $|\phi_{\lambda,\mathbf{k}}\rangle$ are obtained from a tight-binding model[45] that has been mapped from a density functional theory computation. The phase of the wave functions $|\phi_{\lambda,\mathbf{k}}\rangle$ can be chosen arbitrarily, which introduces a gauge freedom to the problem. As a result, some of the microscopic quantities, such as the computed matrix elements ($\mathbf{d}_{\mathbf{k}}^{\lambda,\mu}$, $\mathcal{A}_{\mathbf{k}}^{e,h}$ and $V_{\mathbf{k},\mathbf{k}'}^{\lambda,\mu}$) and the microscopic polarization $P_{\mathbf{k}}$ will be gauge dependent. Computing all these quantities directly from the wave functions guarantees that all phases are consistently implemented and ensures formal gauge invariance of the SBEs and all physical observables, such as the macroscopic polarization $\mathbf{P}(t) = \frac{1}{S}\sum_{\mathbf{k}}\mathbf{d}_{\mathbf{k}}^{h,e}P_{\mathbf{k}}$ relevant for the emission. When $|\phi_{\lambda,\mathbf{k}}\rangle$ are numerically computed, their phase can be random, which is problematic for the numerical evaluation of the gradient terms in equation (1). We settle the phases using the twisted parallel-transport gauge[46] in the direction of the THz field, which minimizes the Berry connection in the respective direction. The SBEs and doublets are solved for two pairs of valence and conduction bands on the full two-dimensional Brillouin zone, which is discretized using a rhombic grid with up to $117 \times 117 = 13{,}689$ $\mathbf{k}$ points, and it is confirmed that the results converge at $69 \times 69 = 4{,}761$ $\mathbf{k}$ points.

Wigner representation

Whereas all relevant HSB aspects can be computed directly from the macroscopic polarization density, $\mathbf{P}(t) = \frac{1}{S}\sum_{\mathbf{k}}\mathbf{d}_{\mathbf{k}}^{h,e}P_{\mathbf{k}}(t)$ within normalization area S, microscopic $P_{\mathbf{k}}(t)$ distributions can elucidate the quantum dynamics details of extreme lightwave excitations. We find it particularly intuitive to present the $P_{\mathbf{k}}(t)$ dynamics via a Wigner function[47]

$$W(x,k) = \frac{1}{\mathcal{N}\pi}\int dq\int dj\ P_{(k+q)\hat{\mathbf{x}}+j\hat{\mathbf{y}}}^{*}P_{(k-q)\hat{\mathbf{x}}+j\hat{\mathbf{y}}}\,e^{-2iqx} \quad (3)$$

that is tailored to reveal the phase-space dynamics in the direction of the THz field, along the $\hat{\mathbf{x}}$ (opposed to $\hat{\mathbf{y}}$) unit vector. With a proper norm $\mathcal{N}$, $\langle x\rangle = \int dx\,dk\,x\,W(x,k)$ and $\langle k\rangle = \int dx\,dk\,k\,W(x,k)$, we reduce the full phase-space representation to a simple ($\langle x\rangle(t)$, $\langle k\rangle(t)$) trajectory, shown in Fig. 3. To gain direct information for the HSB-relevant coherences, we high-pass filter $P_{\mathbf{k}}^{HSB}(t) = \int dt' P_{\mathbf{k}}(t)G(t-t')$ with a kernel $G(t)$ that includes only the frequency range collected in the spectrally integrated HSB intensity I_{HSB}, presented in Figs. 1, 2 and 4 in the main text. The HSB Wigner function, $W_{HSB}(x,k)$, is obtained by replacing $P_{\mathbf{k}}$ by $P_{\mathbf{k}}^{HSB}$ in equation (3).

Connection of HSB emission, recollisions and Coulomb effects

Figure 1a,b outlines how many-body interactions affect the timing of e–h recollisions and HSB emission. To illustrate how these key aspects are precisely connected, Extended Data Fig. 5a shows the actual time evolution of the HSB intensity, defined by the HSB-relevant polarization, $\mathbf{P}^{HSB}(t) \equiv \frac{1}{S}\sum_{\mathbf{k}}\mathbf{d}_{\mathbf{k}}^{h,e}P_{\mathbf{k}}^{HSB}(t)$, which our QDCE computations provide for monolayer (blue line) and bulk (orange line) WSe_2. In both cases, very little emission is observed until the HSB burst at time T_{coll}, which clearly illustrates the distinct delay sequence from interband generation and THz acceleration to e–h recollision. As discussed in the main text, many-body correlations modify the e–h dynamics and lead to $T_{coll}^{ML} = 12.6$ fs for the monolayer and $T_{coll}^{bulk} = 18.6$ fs for the bulk, which implies a 6.0 fs change in collision. This difference affects the optimal t_{ex} as well, such that Coulomb effects can be directly measured via our chronoscopy concept.

To further confirm the connection between excitonic binding energy, HSB emission bursts and recollision times, we have constructed the HSB Wigner function, $W_{HSB}(x,k)$, from $P_{\mathbf{k}}^{HSB}(t)$ at the peak of the HSB emission. Extended Data Fig. 5b–e shows the corresponding $W_{HSB}(x,k)$ at the respective recollision times. For the monolayer, $W_{HSB}(x,k)$ exhibits a major recollision contribution (red circle) at $x = 0$ at $t = T_{coll}^{ML} = 12.6$ fs (Extended Data Fig. 5b), whereas only collision debris remains at a later time $t = 18.6$ fs (Extended Data Fig. 5c). A similar synchronization of recollision and emission bursts is observed for the bulk; for $t = 12.6$ fs, $W_{HSB}(x,k)$ has no overlap with the expected recollision region $x = 0$ (Extended Data Fig. 5d), whereas clear recollision contributions (red circle) are present at $t = T_{coll}^{bulk} = 18.6$ fs (Extended Data Fig. 5e).

All-optical switching of the Coulomb interaction

The SBEs systematically describe the excitonic attraction between electrons and holes via the product of the Coulomb matrix element $V^{e,h}_{\mathbf{k},\mathbf{k}'}$ within $\Omega_{\mathbf{k}}$ of equation (2) and the Pauli-blocking contribution $(1-f^{e}_{\mathbf{k}}-f^{h}_{\mathbf{k}})$, which describes how the presence of fermionic electrons and holes excludes other fermions from the same wave vector **k**. In other words, the effective Coulomb interaction $W_{\mathbf{k},\mathbf{k}'} \equiv (1-f^{e}_{\mathbf{k}}-f^{h}_{\mathbf{k}})\,V^{e,h}_{\mathbf{k},\mathbf{k}'}$ depends on the excitation, and elevated e–h occupation levels can even quench the Coulombic effects when inversion, $(1-f^{e}_{\mathbf{k}}-f^{h}_{\mathbf{k}}) \to 0$, is approached. As explained in the main text, circularly polarized light excitation creates $f^{e}_{\mathbf{k}}$ and $f^{h}_{\mathbf{k}}$ to occupy a single valley of the WSe_2 monolayer, whereas linearly polarized NIR light excites both valleys equally, halving the $f^{e}_{\mathbf{k}}$ and $f^{h}_{\mathbf{k}}$ occupations. Thus, the same pump intensity produces a weaker $W_{\mathbf{k},\mathbf{k}'}$ for circular than for linear excitation due to Pauli blocking. Figure 4 in the main text demonstrates how to exploit this fundamental property for an experimental switching of exciton binding, to directly measure the influence of Coulomb interaction on attosecond clocking.

Accuracy of attosecond clocking with finite-duration NIR pulses

To understand how the duration of the optical generation pulse affects the accessible timing, we computed I_{HSB} for four representative NIR pulse durations $\tau_{\mathrm{NIR}} = 7.2$ fs (Extended Data Fig. 6, dark red line), $\tau_{\mathrm{NIR}} = 8.6$ fs (dark blue line), $\tau_{\mathrm{NIR}} = 10$ fs (light red line) and $\tau_{\mathrm{NIR}} = 11.5$ fs (light blue line). The NIR pulse duration controls the depth of the modulations in I_{HSB}, but affects much less the timing of the HSB peaks. To quantify the actual dependence of the clocking precision on τ_{NIR}, we define the change, $\Delta_{\mathrm{sc}} \equiv \delta_{\mathrm{sc}}(\tau_{\mathrm{NIR}}) - \delta_{\mathrm{sc}}(8.6\ \mathrm{fs})$, for the subcycle delay with respect to the excitation scenario with $\tau_{\mathrm{NIR}} = 8.6$ fs (Extended Data Table 1). We observe that Δ_{sc} saturates for $\tau_{\mathrm{NIR}} < 10$ fs, entailing a change of less than 50 as at the largest E_{THz} peak (second peak), and less than 90 as for the average Δ_{sc} of the three largest peaks. This confirms that our chronoscopy concept can detect even the slightest changes of subcycle dynamics down to attosecond precision.

Difference between HSB and high-harmonic generation

Whereas high-harmonic generation relies on the complex interplay between interband polarization and intraband acceleration, HSB generation sharply separates those two steps by using a resonant excitation pulse. This way, even comparably weak driving fields can lead to a significant emission of high-energy radiation. Our QDCE calculations reveal that HSB generation is three orders of magnitude more efficient than high-harmonic generation for our field strengths of not more than 6.2 MV cm^{-1}. Therefore, non-resonant interband excitations by our driving field, which could influence the subcycle dynamics of coherent polarization as well as the emission of high-harmonic radiation[48,49], are strongly suppressed. Additionally, coherent excitons are excited over the direct bandgap at the K point in both the monolayer and the bulk case, even though the bulk conduction band minimum lies between the K and the Γ point. Generally, HSB generation is based on e–h recollisions that can occur even if the excursion in momentum space explores only a fraction of the Brillouin zone[26]. As the band structures around the K point are comparable for the bulk and the monolayer cases, the nature of the bandgap does not dramatically change the dynamics in our experiment.

Dynamical versus constant-dephasing effects on HSB spectra

As discussed in the main text, computations with constant-dephasing times fail to reproduce experimental features, such as the HSB spectral shape and intensity. To further illustrate this fact, Extended Data Fig. 7a presents the computed spectra $I_{\mathrm{HSB}}(h\nu)/I_{\mathrm{NIR}}$ for the full QDCE computation (shaded area), and three constant-dephasing computations with $\tau = 21.9$ fs (red line), 13.2 fs (purple line) and 8.2 fs (blue line). Only the results of the full QDCE match with the experiment. All constant-dephasing computations produce HSB spectra that differ significantly from the full QDCE result above 2 eV, particularly for $\tau = 21.9$ fs and 8.2 fs. To quantify pure shape deviations, we also plot the ratio of the HSB spectral intensities obtained from QDCE and constant-dephasing computations in Extended Data Fig. 7b. The constant-dephasing approximation introduces sharp additional oscillations, which are not present in QDCE computations and the experimental data.

Microscopically, for early delay times, the density of coherent excitons, $n_{\mathrm{coh}}(t)$, in our full QDCE computations (Extended Data Fig. 7c, grey area) closely follows the simulations with the largest dephasing time ($\tau = 21.9$ fs, red line), until the peak of $n_{\mathrm{coh}}(t)$ is reached. After that, the coherences from the full QDCE start decaying much faster, approaching the limit of our computations with $\tau = 8.2$ fs (blue line). In other words, the full microscopic scattering changes its nature from a slow to a fast decay because the NIR pulse excites 'slowly' decaying 1*s* exciton coherences, whereas THz excitation induces other states, which decay much faster, as predicted in ref. [42]. This intricate many-body feature has drastic consequences for the HSB spectra—a constant-dephasing computation cannot explain the measured HSB features because the total decay is not reducible to a single, static constant.

Summary of attosecond timing contributions

By varying single parameters separately in our QDCE computations, we can quantify how much each can shift the subcycle delay δ_{sc}. For the exciton binding energy this can be easily achieved by multiplying the strength of the Coulomb interaction $V_{\mathbf{k}}$ artificially by a suppression factor s_{C}. As a result of the altered $s_{\mathrm{C}}V_{\mathbf{k}}$, only the Coulombic effects are changed, which we quantify through the absolute value of the 1*s* exciton binding energy E_{1s}. We observe that δ_{sc} decreases roughly at a rate of −9 as meV^{-1} with increasing E_{1s}, for both the bulk (Extended Data Fig. 8, orange line) and the monolayer (blue line). The actual subcycle delay computed for the bulk amounts to $\delta_{\mathrm{sc}} = 2.3$ fs (orange sphere), whereas the monolayer with artificially matched $E_{1s} = 60$ meV yields $\delta_{\mathrm{sc}} = 3.8$ fs, which is 1.5 fs above the bulk delay. Both cases also produce an almost parallel but shifted E_{1s} dependence, indicating that this 1.5 fs shift originates from changes to the band structure that are included in the actual bulk computation. Our analysis shows that the delay shift of 2.1 fs owing to the reduced Coulomb interaction in the bulk is 40% higher than the shift induced by differences in the band structure. The observed subcycle delay difference between monolayer and bulk WSe_2 is therefore dominated by changes to the Coulomb interaction. Additionally, we find that the THz field strength can change δ_{sc} by 2 fs (Fig. 3a) and Pauli blocking induces a shift of up to 1 fs as the NIR fluence is varied (Fig. 4e).

Data availability

Source data are provided with this paper. The data supporting the findings of this study are available from the corresponding authors upon request. All other data needed to evaluate the conclusions in the paper are present in the paper or the Methods section.

41. Meierhofer, M. et al. Interferometric carrier-envelope phase stabilization for ultrashort pulses in the mid-infrared. Preprint at https://arxiv.org/abs/2207.10073 (2022).
42. Kira, M. & Koch, S. W. Many-body correlations and excitonic effects in semiconductor spectroscopy. *Prog. Quantum Electron.* **30**, 155–296 (2006).
43. Kira, M. Coherent quantum depletion of an interacting atom condensate. *Nat. Commun.* **6**, 6624 (2015).
44. Kira, M. & Koch, S. W. Quantum-optical spectroscopy in semiconductors. *Phys. Rev. A* **73**, 013813 (2006).
45. Fang, S. et al. Ab initio tight-binding Hamiltonian for transition metal dichalcogenides. *Phys. Rev. B* **92**, 205108 (2015).
46. Vanderbilt, D. *Berry Phases in Electronic Structure Theory: Electric Polarization, Orbital Magnetization and Topological Insulators* (Cambridge Univ. Press, 2018).
47. Wigner, E. On the quantum correction for thermodynamic equilibrium. *Phys. Rev.* **40**, 749–759 (1932).
48. Heide, C. et al. Probing electron-hole coherence in strongly driven 2D materials using high-harmonic generation. *Optica* **9**, 512–516 (2022).

49. Nagai, K. et al. Effect of incoherent electron-hole pairs on high harmonic generation in atomically thin semiconductors. Preprint at https://arxiv.org/abs/2112.12951 (2021).

Acknowledgements We thank K.-Q. Lin, H. Petek and N. Hofmann for assistance and helpful discussions. The work in Regensburg has been supported by the Deutsche Forschungsgemeinschaft (DFG, German Research Foundation) through Project ID 422 314695032-SFB 1277 (Subproject A05) as well as Research Grant HU1598/8. Work in Ann Arbor has been supported by ARO through Award W911NF1810299, W.M. Keck Foundation and College of Engineering Blue Sky Research Program.

Author contributions M. Kira and R.H. conceived and supervised the study. J.F., M.M., D.A., C.P.S. and R.H. carried out the experiment and analysed the data. F.S., M.L., A.G. and M. Knorr provided, processed and characterized the samples. M.B. and M. Kira developed and performed the many-body computations and analysed the data. J.F., M.B., M. Kira and R.H. wrote the manuscript with contributions from all authors.

Competing interests The authors declare no competing interests.

Additional information

Supplementary information The online version contains supplementary material available at https://doi.org/10.1038/s41586-022-05190-2.

Correspondence and requests for materials should be addressed to D. Afanasiev, M. Kira or R. Huber.

Peer review information *Nature* thanks Michael Sentef, Liang Luo and Koichiro Tanaka for their contribution to the peer review of this work.

Reprints and permissions information is available at http://www.nature.com/reprints.

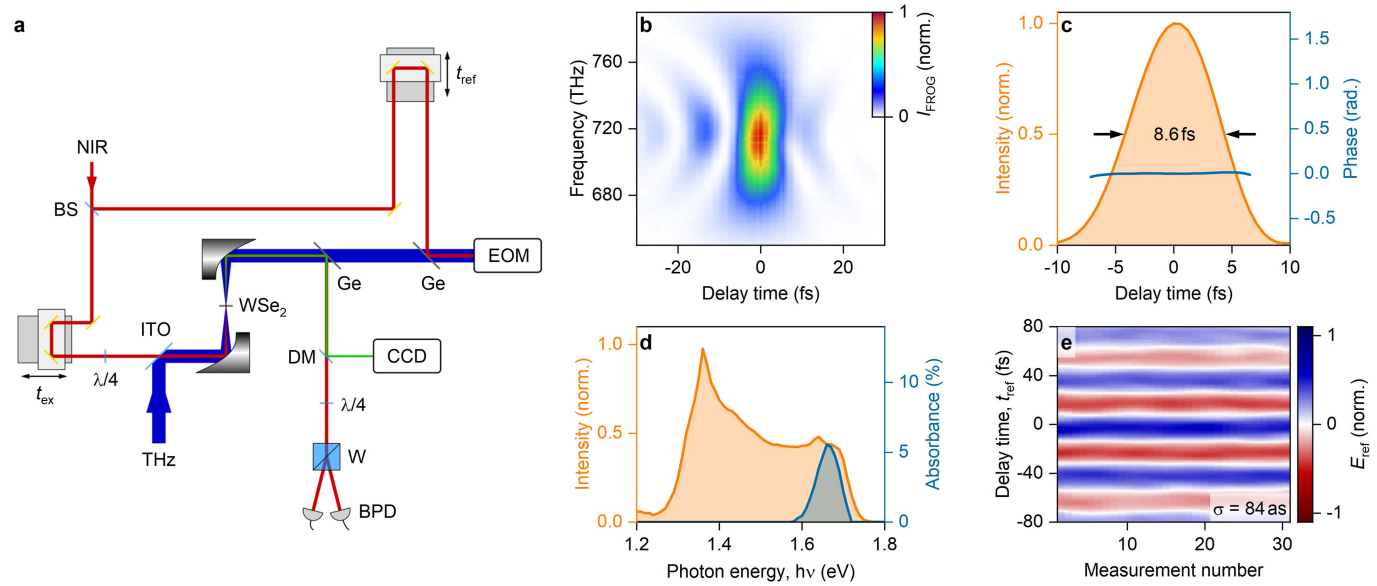

Extended Data Fig. 1 | Schematic of the experimental setup. a, The 8.6-fs-NIR pulse train is split into two branches. The first one passes a quarter wave plate (λ/4) and is overlapped with the THz field with an indium tin oxide-coated window (ITO) before both pulses are focused onto a GaSe crystal for EOS or the WSe_2 sample to generate HSB. The remaining excitation light and the emerging HSB radiation are collimated and separated from the THz radiation with a germanium wafer (Ge). With a dichroic mirror (DM), the HSB radiation is sent into a spectrometer (CCD), while the polarization state of the transmitted NIR pulse can be analysed by a quarter wave plate, a Wollaston prism (W), and a balanced pair of photodiodes (BPD). The remaining THz field is overlapped with the second NIR branch to constantly monitor the electro-optic signal (EOM). **b**, Measured SHG-FROG spectrogram and **c**, reconstructed temporal shape of the NIR light with a pulse duration of 8.6 fs. **d**, Comparison between excitation spectrum (orange) and absorbance (blue) of monolayer WSe_2. The high-energy edge of the excitation spectrum is chosen to be resonant with the monolayer 1s transition. **e**, Waterfall plot of successive EOS measurements with the reference beam line. The electric field of the reference THz waveform corresponds to the colour scale. Fitting the temporal position of the recorded transients reveals a standard deviation of only σ = 84 as, attesting to the excellent stability of the setup during a measurement.

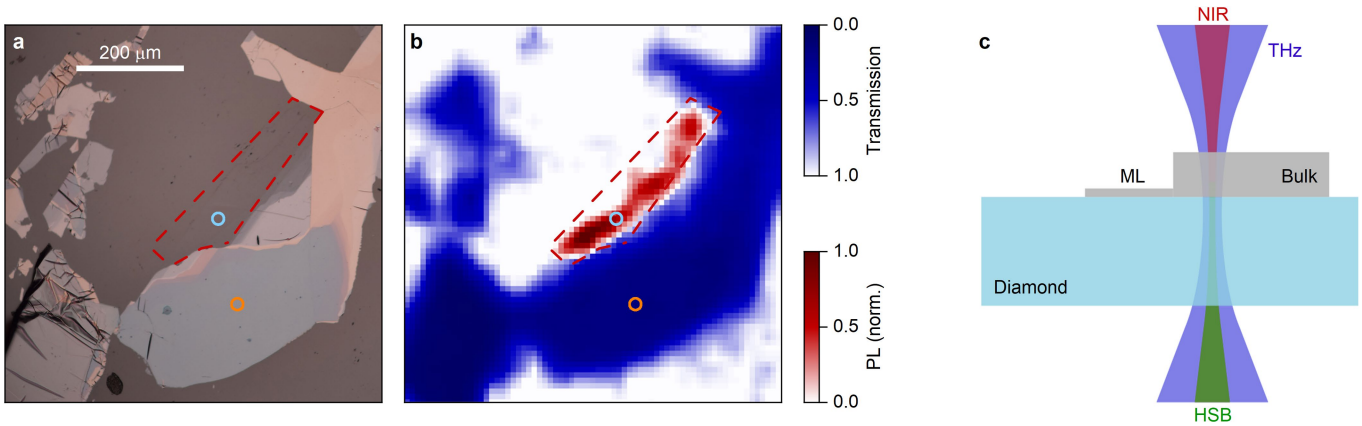

Extended Data Fig. 2 | Identifying monolayer and bulk WSe_2. **a**, Optical microscopy picture of the exfoliated sample on a diamond substrate. The monolayer part of the WSe_2 crystal is indicated by the red dashed line. Circles (diameter corresponds to the NIR spot size in focus) show the spots used for the monolayer (blue) and bulk (orange) measurements presented in the main text. **b**, Photoluminescence (red colour map) and transmission (blue colour map) of the sample using a continuous-wave laser with a centre wavelength of 532 nm. **c**, Schematic cross-section of the WSe_2 sample consisting of a bulk and monolayer (ML) part next to each other on a diamond substrate. The incident light (NIR and THz) hits the sample from the WSe_2 side. Remaining NIR and THz radiation as well as the emitted HSB radiation are transmitted through the diamond substrate.

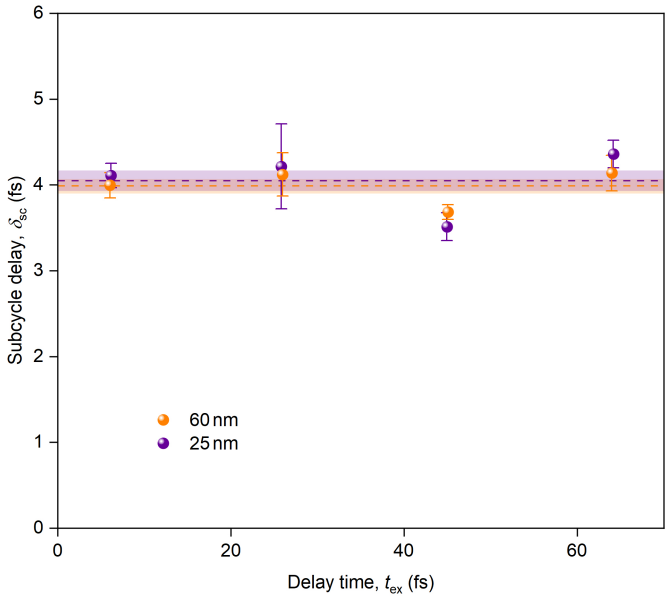

Extended Data Fig. 3 | Dependence of the subcycle delay on the sample thickness. Measured subcycle delay δ_{sc} and its standard error for different spots on the WSe_2 sample with $E_{peak} = 6.2\,MV\,cm^{-1}$ and $\Phi_{NIR} = 12\,\mu J\,cm^{-2}$. 60 nm (orange) and 25 nm (purple) thick areas of the crystal yield the same averaged value $\langle\delta_{sc}\rangle$ (dashed line) within the averaged margin of error (shaded area).

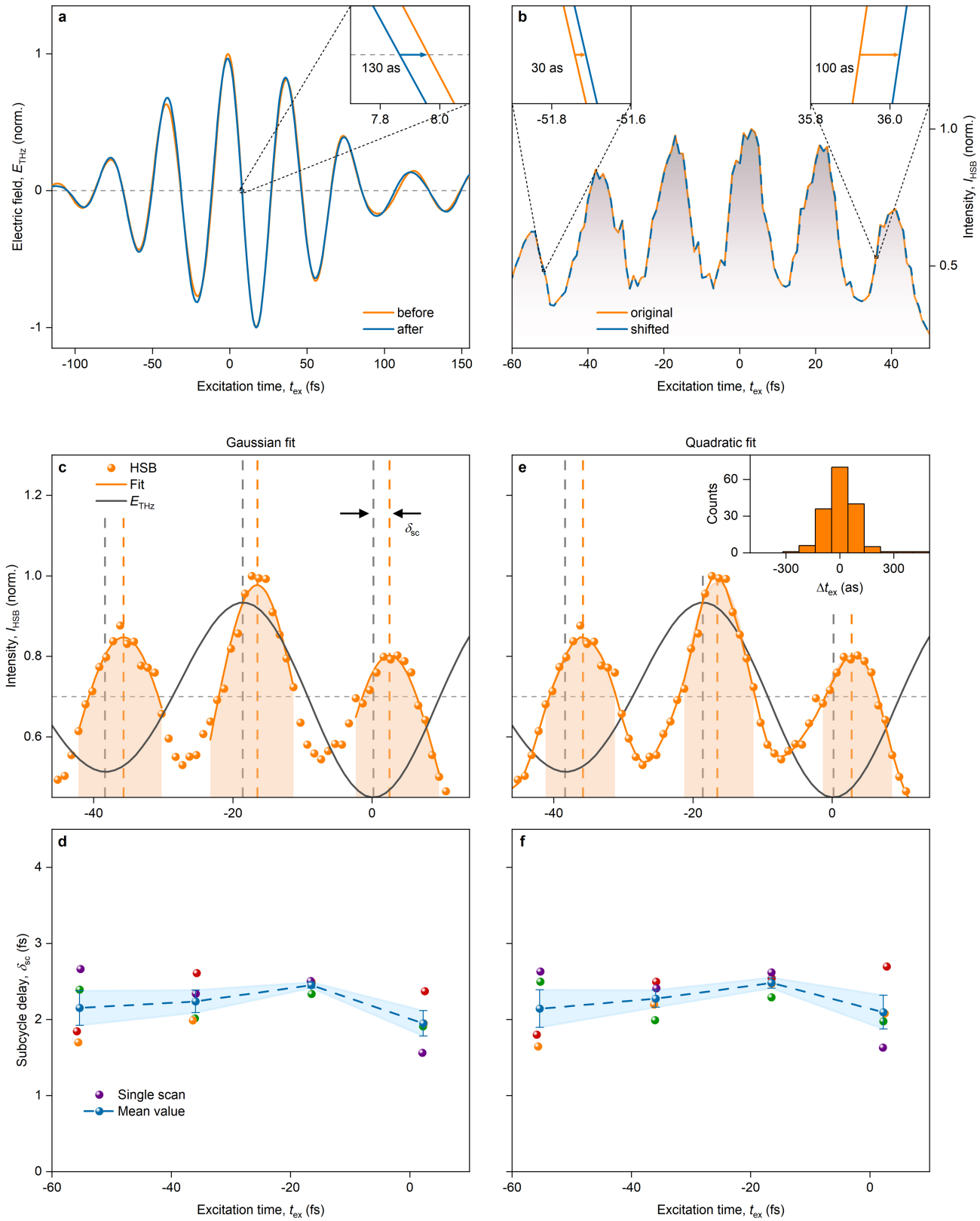

Extended Data Fig. 4 | See next page for caption.

Extended Data Fig. 4 | Data analysis and calculation of error bars. **a**, Recorded transient before (orange solid line) and after (blue solid line) a single scan of the HSB spectrogram. The inset shows a close-up of a field zero-crossing, revealing a shift of 130 as of the driving field during a measurement. **b**, Spectrally integrated trace of a single HSB scan as recorded (orange) and after compensation of the temporal drift (blue). Its time axis is stretched or squeezed (blue) in accordance with the temporal shift correction in **a**. Insets: Zoom-in on I_{HSB} illustrating the drift compensation for early (left panel) and late (right panel) injection times. **c**, **e**, Peaks of the corrected HSB emission (orange spheres) are fitted using Gaussian (**c**) or quadratic (**e**) functions (orange solid lines) in a small temporal window (orange shaded area) to determine their exact temporal position. The subcycle delay, δ_{sc}, is calculated as the timing difference between I_{HSB} and E_{THz} (grey) peaks. Inset in **e**: histogram of the deviation of the interpolated curve (line) from the raw data (dots), yielding a noise-limited time resolution of 100 as. **d**, **f**, Extracted subcycle delay from **c** and **e** for four consecutive scans (coloured spheres). By averaging, their mean value (blue spheres) as well as their standard error (indicated by the blue shaded area) are determined.

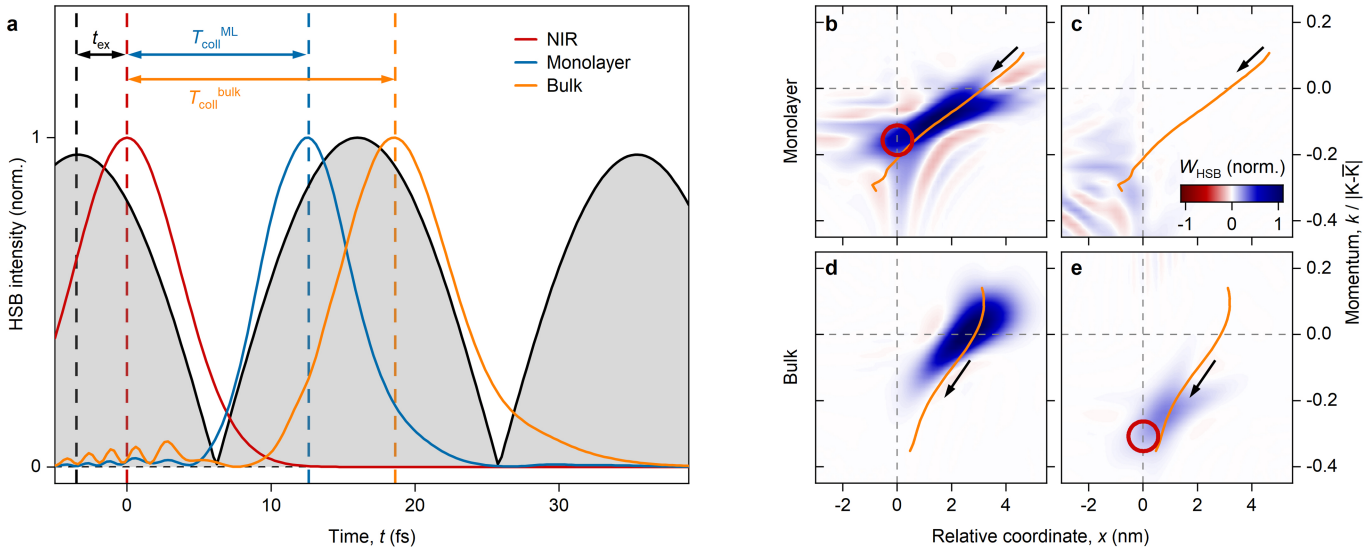

Extended Data Fig. 5 | Synchronized timing of *e*–*h* recollisions and HSB emission. a, Time-resolved computed HSB emission intensity for monolayer (blue line) and bulk (orange line) WSe_2. Coherent excitons are created by an 8.6 fs NIR pulse (intensity envelope, red line) at time t_{ex} after the peak of the THz field ($|E_{THz}|$, grey shaded area). The HSB emission peaks (vertical dashed lines) at $T_{coll}^{ML} = 12.6$ fs after the excitation for monolayer and at $T_{coll}^{bulk} = 18.6$ fs for bulk WSe_2, respectively. **b**–**e**, HSB Wigner functions $W_{HSB}(x,k)$ (contours) at times $t = 12.6$ fs and $t = 18.6$ fs for monolayer and bulk WSe_2. Orange lines show the dynamics of the centroid of the Wigner function.

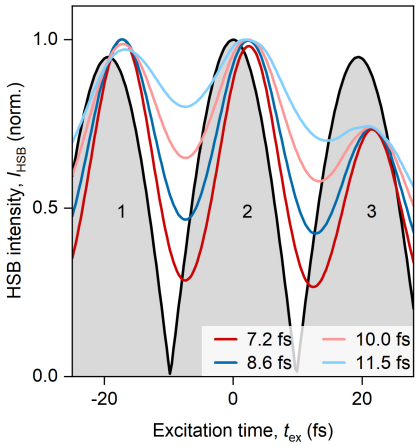

Extended Data Fig. 6 | Predicted HSB intensity as a function of the NIR pulse duration. Computed HSB intensity I_{HSB} as a function of the NIR excitation time for pulse durations of τ_{NIR} = 7.2 fs (dark red line), 8.6 fs (dark blue line), 10 fs (light red line), and 11.5 fs (light blue line). The shaded area denotes the driving field $|E_{THz}|$ whose three largest peaks are labelled.

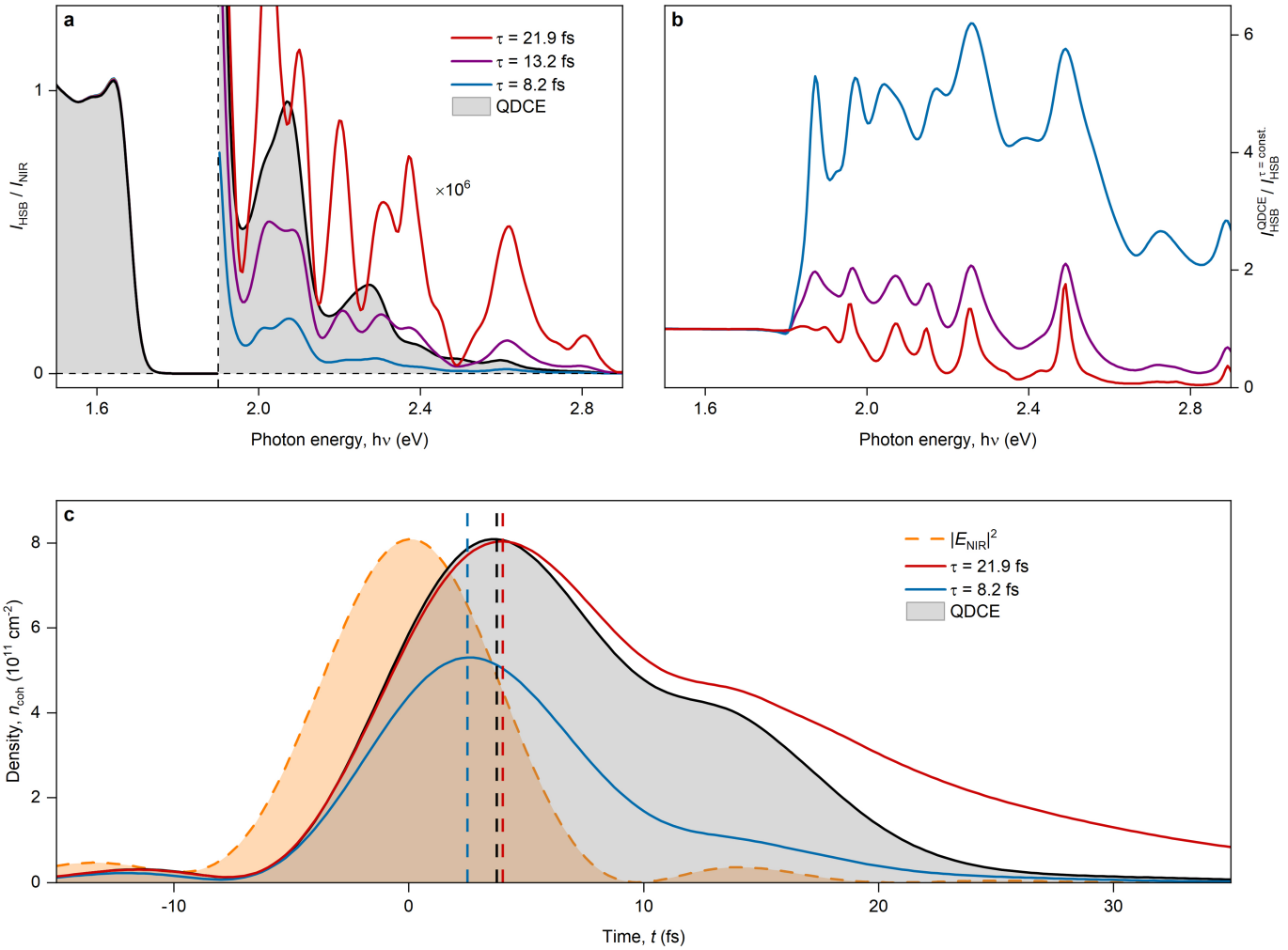

Extended Data Fig. 7 | HSB spectra for constant dephasing times. **a**, Computed HSB spectra of the full QDCE approach (grey shaded area) compared to computations with different constant dephasing times τ (lines). The data are multiplied by a factor of 10^6 at energies $h\nu > 1.9$ eV, for visibility. **b**, Ratio of the spectrum from the full QDCE computation with each of the constant-dephasing computations. **c**, Density of coherent excitons as function of time for the full QDCE computation (grey area) and two constant-dephasing calculations with $\tau = 21.9$ fs (red line) and $\tau = 8.2$ fs (blue line) after excitation (orange shaded area, NIR pulse envelope). The vertical dashed lines indicate peak densities.

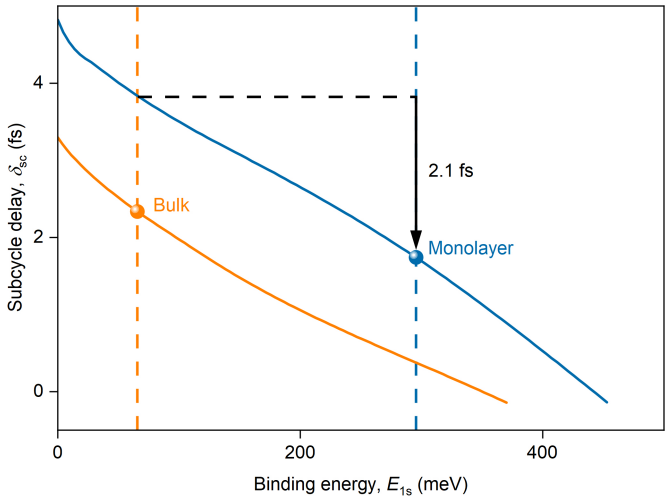

Extended Data Fig. 8 | Role of Coulomb correlations on the subcycle delay. Computed subcycle delay for bulk (orange) and monolayer (blue) WSe_2 as a function of the exciton binding energy resulting from a Coulomb interaction suppressed artificially, while keeping all other parameters fixed. Orange and blue dashed vertical line: exciton binding energy E_{1s} of bulk (E_{1s} = 60 meV) and monolayer (E_{1s} = 295 meV) WSe_2, respectively. The arrow marks the subcycle-delay shift of 2.1 fs due to increased excitonic binding.

Extended Data Table 1 | Predicted precision of subcycle delay as a function of the NIR pulse duration

τ_{NIR}	2^{nd}-peak Δ_{sc}	Mean Δ_{sc}
7.2 fs	36 as	49 as
10.0 fs	-47 as	-84 as
11.5 fs	-207 as	-369 as

The change of the subcycle delay with respect to excitation with τ_{NIR} = 8.6 fs is tabulated for the largest peak (see Extended Data Fig. 6) and the average of the three largest peaks of $|E_{THz}|$.